J. Fluid Mech. (1998), *vol.* 368, *pp.* 263–289. Printed in the United Kingdom

Double-diffusive convection instability in a vertical porous enclosure

By M. MAMOU, P. VASSEUR AND E. BILGEN

Department of Mechanical Engineering, Ecole Polytechnique, University of Montreal, C.P. 6079, Succ. "Down-Town" Montreal, Quebec, H3C 3A7, Canada
e-mail: vasseur@meca.polymtl.ca

(Received 16 June 1997 and in revised form 27 February 1998)

The Galerkin and the finite element methods are used to study the onset of the double-diffusive convective regime in a rectangular porous cavity. The two vertical walls of the cavity are subject to constant fluxes of heat and solute while the two horizontal ones are impermeable and adiabatic. The analysis deals with the particular situation where the buoyancy forces induced by the thermal and solutal effects are opposing each other and of equal intensity. For this situation, a steady rest state solution corresponding to a purely diffusive regime is possible. To demonstrate whether the solution is stable or unstable, a linear stability analysis is carried out to describe the oscillatory and the stationary instability in terms of the Lewis number, Le, normalized porosity, ε, and the enclosure aspect ratio, A. Using the Galerkin finite element method, it is shown that there exists a supercritical Rayleigh number, R_{TC}^{sup}, for the onset of the supercritical convection and an overstable Rayleigh number, R_{TC}^{over}, at which overstability may arise. Furthermore, the overstable regime is shown to exist up to a critical Rayleigh number, R_{TC}^{osc}, at which the transition from the oscillatory to direct mode convection occurs. By using an analytical method based on the parallel flow approximation, the convective heat and mass transfer is studied. It is found that, below the supercritical Rayleigh number, R_{TC}^{sup}, there exists a subcritical Rayleigh number, R_{TC}^{sub}, at which a stable convective solution bifurcates from the rest state through finite-amplitude convection. In the range of the governing parameters considered in this study, a good agreement is observed between the analytical predictions and the finite element solution of the full governing equations. In addition, it is found that, for a given value of the governing parameters, the converged solution can be permanent or oscillatory, depending on the porous-medium porosity value, ε.

1. Introduction

This paper reports a theoretical study of natural thermosolutal convection in a binary fluid-saturated porous medium. Relative to a large volume of published studies on this phenomenon in pure fluids, the thermosolutal convection in porous media has received only limited attention, although it has interesting engineering applications: the migration of moisture through the air contained in fibrous insulation, grain storage installations, food processing and the underground spreading of chemical pollutants. Double-diffusive flows through porous media are also of interest in geophysical systems, electrochemistry and metallurgy.

A comprehensive review of the literature concerning double-diffusive natural convection in a fluid-saturated porous medium may be found in the book by Nield &

Bejan (1992). Numerical and analytical solutions were obtained by Trevisan & Bejan (1985, 1986), Alavyoon (1993), Alavyoon, Masuda & Kimura (1994), Lin (1993), Goyeau, Songbe & Gobin (1996), Mamou *et al.* (1995*b*) and Mamou (1998), for the case of a rectangular cavity under various thermal and solutal boundary conditions. In these studies both augmenting and opposing horizontal temperature and concentration gradients were considered. The results indicate that the cell patterns and the characteristics of heat and solute transfer in the flows are substantially influenced by the governing parameters: the thermal Rayleigh number, R_T, the ratio of the buoyancy forces, N, and the Lewis number, Le, for a given aspect ratio, A. Furthermore, for opposing buoyancy forces ($N < 0$), using different initial conditions, Mamou, Vasseur & Bilgen (1995*a*) showed that there are multiple convective solutions with different multicellular flow patterns. In addition to the above studies, the double-diffusive phenomenon in non-homogeneous and anisotropic porous media has been investigated by Mehta & Nandakumar (1987) and Nguyen, Pack & Douglass (1994) respectively.

For the case of opposing and equal buoyancy forces, $N = -1$, Trevisan & Bejan (1986) demonstrated that when $Le = 1$ the temperature and concentration fields are identical and the only possible solution is that corresponding to the pure diffusive regime. Alavyoon (1993) and Alavyoon *et al.* (1994), have developed an analytical solution showing that when $Le = 1$ the problem does not belong to the class of problems that are described as double-diffusive phenomena. Also, it was demonstrated that, when $N = -1$, the pure diffusive regime is an exact solution of the problem even when $Le \neq 1$. However, when the Lewis number is not equal to unity there is no reason to expect that the rest state remains unconditionally stable. This has been demonstrated by Krishnan (1989) and Gobin & Bennacer (1994) for the case of a binary fluid layer, bounded by vertical walls kept at constant and different temperatures and concentrations. Recently, Nithiarasu, Seetharamu & Sundararajan (1996) studied a similar problem on the basis of the generalized non-Darcy model. Their numerical results lead to the conclusion that, when $N = -1$, the convective flow disappears since the buoyancy forces cancel each other. As a result, the heat and mass transfer are governed by pure diffusion. This point was demonstrated by the numerical results obtained by Trevisan & Bejan (1985). All the above investigations are restricted to the case of $\varepsilon = 1$. However, in practical applications, ε is smaller than unity and the effect of this parameter on the solution is expected to be significant. Indeed, in the present study, the porosity of the porous medium was found to have a strong influence on the flow structure and on the heat and mass transfer rates and there exists a threshold for the convective motion even when $Le = 1$.

In this work, a new numerical technique based on the Galerkin and the finite element methods is developed to study the convective instability problem within a rectangular porous enclosure subject to horizontal gradients of temperature and solute concentration. The particular case of $N = -1$, for which a basic rest state solution may exist, will be considered. Using a linear stability analysis, the oscillatory instability, in which a small perturbation grows in an oscillatory manner, and the stationary instability, in which the perturbation grows in a monotonic manner, will be investigated in terms of the governing parameters. On the other hand, in the limit of a slender enclosure, an analytical nonlinear theory is developed to study the finite-amplitude convection instability and to determine the onset of subcritical convection. For comparison, a finite element simulation of the full governing equations is employed.

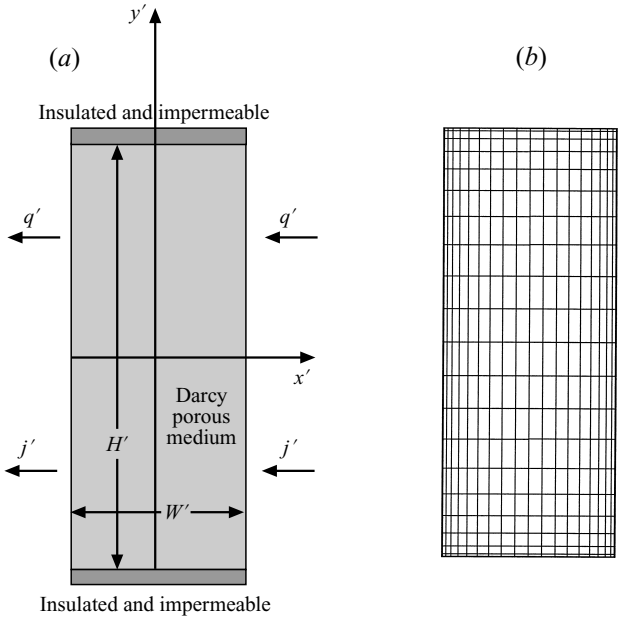

FIGURE 1. (*a*) Physical system, (*b*) computational domain.

The content of the present paper is structured as follows. In the next section (§ 2) we define the physical system and introduce the mathematical model of the problem. In § 3 we develop a finite element solution of the governing equations for a finite enclosure aspect ratio. For a slender enclosure, an analytical finite-amplitude solution based on the parallel flow approximation is derived. In § 4 we present a numerical linear stability analysis, on the basis of the Galerkin and the finite element methods, to study the oscillatory and the direct modes of convection. Finally, conclusions are presented in the last section § 5.

2. Mathematical formulation

The physical domain under study is a two-dimensional vertical porous layer of height H' and width W' (see figure 1). The two long sidewalls are subject to horizontal uniform fluxes of heat and mass per unit area, q' and j', respectively, while the short endwalls are insulated and impermeable. The porous matrix is assumed to be homogeneous and isotropic and the appropriate Darcy model is used. The Soret and Dufour effects are negligible as discussed, for instance, by De Groot & Mazur (1962) and Bergman & Shrinivasan (1989).

The binary fluid that saturates the porous matrix is modelled as a Boussinesq fluid whose density, ρ, varies linearly with temperature T' and concentration S':

$$\rho = \rho_0[1 - \beta_T(T' - T'_0) - \beta_S(S' - S'_0)], \tag{2.1}$$

where ρ_0 is the fluid density at temperature $T' = T'_0$ and concentration $S' = S'_0$, and β_T and β_S are the thermal and concentration expansion coefficients, respectively. The subscript $_0$ refers to conditions at the origin of the coordinate system.

In the present study, the case of equal and opposing solutal and thermal buoyancy forces is considered, such that

$$N = \frac{\beta_S \; j' \; \kappa}{\beta_T \; q' D} = -1, \tag{2.2}$$

where κ and D are the thermal conductivity of the saturated porous medium and the mass-averaged diffusivity through the fluid mixture. Thus, in the present model, the concentration and temperature gradients tend to drive the flow clockwise and counterclockwise respectively.

The following dimensionless variables (primed quantities are dimensional) are used:

$$\left.\begin{aligned} &(x,\ y) = \left(\frac{x'}{W'},\ \frac{y'}{W'}\right), \quad u = u' \; \frac{W'}{\alpha}, \quad v = v' \; \frac{W'}{\alpha}, \quad t = t' \; \frac{\alpha}{\sigma W'^2}, \\ &T = \frac{T' - T'_0}{\Delta T^*}, \quad \Delta T^* = \frac{q' W'}{\kappa}, \quad S = \frac{S' - S'_0}{\Delta S^*}, \quad \Delta S^* = \frac{j' W'}{D}, \end{aligned}\right\} \tag{2.3}$$

where u' and v' are the volume-averaged velocity components, t' is the time, $\alpha = \kappa/(\rho C)_f$ the thermal diffusivity of the porous medium, $\sigma = (\rho C)_p/(\rho C)_f$ the saturated porous medium to fluid heat capacity ratio, while ϕ is the porosity of the porous matrix.

In the forgoing analysis, the stream function formulation is introduced in the mathematical model. In order to satisfy the continuity equation, the stream function Ψ is defined such that

$$u = \frac{\partial \Psi}{\partial y}, \quad v = -\frac{\partial \Psi}{\partial x}. \tag{2.4}$$

In the context of the stability analysis that will be discussed in the following sections, it is convenient to consider the pure diffusive solution as a part of the total solution. Thus, we introduce the following transformations:

$$\left.\begin{aligned} \Psi &= \Psi_C + \psi(t, x, y), \\ T &= T_C + \theta(t, x, y), \\ S &= S_C + \varphi(t, x, y), \end{aligned}\right\} \tag{2.5}$$

where the static state of the system is described by

$$\Psi_C = 0, \quad T_C = S_C = x. \tag{2.6}$$

In terms of the above definitions, the dimensionless governing equations expressing conservation of momentum, energy and species reduce to the following equations:

$$\nabla^2 \psi = -R_T \; \left(\frac{\partial \theta}{\partial x} - \frac{\partial \varphi}{\partial x}\right), \tag{2.7}$$

$$\frac{\partial \theta}{\partial t} + \frac{\partial \psi}{\partial y} - J(\psi, \theta) = \nabla^2 \theta, \tag{2.8}$$

$$\varepsilon \frac{\partial \varphi}{\partial t} + \frac{\partial \psi}{\partial y} - J(\psi, \varphi) = \frac{1}{Le} \; \nabla^2 \varphi, \tag{2.9}$$

where J is the usual Jacobian operator:

$$J(f, h) = \frac{\partial f}{\partial x}\frac{\partial h}{\partial y} - \frac{\partial f}{\partial y}\frac{\partial h}{\partial x}. \tag{2.10}$$

The dimensionless boundary conditions sketched in figure 1 are

$$\left.\begin{aligned} x = \pm\frac{1}{2}, \quad \psi = \frac{\partial\theta}{\partial x} = \frac{\partial\varphi}{\partial x} = 0, \\ y = \pm\frac{A}{2}, \quad \psi = \frac{\partial\theta}{\partial y} = \frac{\partial\varphi}{\partial y} = 0. \end{aligned}\right\} \tag{2.11}$$

Equations (2.7)–(2.11) indicate that the present problem is governed by four dimensionless parameters, namely the thermal Darcy–Rayleigh number, R_T, the Lewis number, Le, the normalized porosity, ε, and the aspect ratio of the enclosure, A, defined as

$$R_T = \frac{g\ \beta_T\ P\ q'\ W'^2}{\kappa\ \alpha\ \nu}, \quad Le = \frac{\alpha}{D}, \quad \varepsilon = \frac{\phi}{\sigma}, \quad A = \frac{H'}{W'}, \tag{2.12}$$

where P is the permeability of the porous medium, g the acceleration due to gravity, ν the kinematic viscosity of the fluid and ϕ the porosity of the porous matrix.

The normalized porosity, ε, expressed in terms of the porosity of the porous medium, ϕ, and the solid to fluid heat capacity ratio, $\sigma_o = (\rho C)_s/(\rho C)_f$, is given by the following expression:

$$\varepsilon = \frac{\phi}{\phi + (1-\phi)\sigma_o}. \tag{2.13}$$

Since $0 < \phi < 1$ and $\sigma_o > 0$, it is clear that

$$0 < \varepsilon < 1. \tag{2.14}$$

In the present notation, the Nusselt and Sherwood numbers are given respectively by

$$Nu = \frac{q'\ W'}{\kappa\ \Delta T'} = \frac{1}{\Delta T}, \quad Sh = \frac{j'\ W'}{D\ \Delta S'} = \frac{1}{\Delta S}, \tag{2.15}$$

where $\Delta T'$ and $\Delta S'$ are the temperature and concentration differences between the two vertical walls, respectively.

3. Finite-amplitude convection solution

3.1. *Numerical solution*

The governing equations (2.7)–(2.9) with their boundary conditions (2.11) are solved by the finite element method described in the following paragraphs.

3.1.1. *Variational formulation*

Multiplying the momentum equation by $w(x, y) \in H^1(\Omega)$ and the energy and species equations by $\vartheta(x, y) \in H^1(\Omega)$ and then integrating over the physical domain Ω, after using the divergence theorem, the weak formulation of the original equations is obtained in terms of the following integrals:

$$\int_\Omega \nabla\psi \cdot \nabla w \ \mathrm{d}\Omega - \int_\Gamma \frac{\partial\psi}{\partial \boldsymbol{n}} w \ \mathrm{d}\Gamma = \int_\Omega R_T \left(\frac{\partial\theta}{\partial x} - \frac{\partial\varphi}{\partial x}\right) w \ \mathrm{d}\Omega, \tag{3.1}$$

$$\int_\Omega \frac{\partial\theta}{\partial t}\vartheta \ \mathrm{d}\Omega + \int_\Omega \frac{\partial\psi}{\partial y}\vartheta \ \mathrm{d}\Omega - \int_\Omega J(\psi,\theta)\vartheta \ \mathrm{d}\Omega = -\int_\Omega \nabla\theta \cdot \nabla\vartheta \ \mathrm{d}\Omega + \int_\Gamma \frac{\partial\theta}{\partial \boldsymbol{n}}\vartheta \ \mathrm{d}\Gamma, \tag{3.2}$$

$$\int_\Omega \varepsilon \frac{\partial \varphi}{\partial t}\vartheta \, d\Omega + \int_\Omega \frac{\partial \psi}{\partial y}\vartheta \, d\Omega - \int_\Omega J(\psi,\varphi)\vartheta \, d\Omega = -\int_\Omega \frac{1}{Le}\nabla\varphi \cdot \nabla\vartheta \, d\Omega + \int_\Gamma \frac{1}{Le}\frac{\partial \varphi}{\partial \boldsymbol{n}}\vartheta \, d\Gamma, \tag{3.3}$$

where $w(x, y)$ and $\vartheta(x, y)$ are the admissible functions satisfying the boundary conditions (2.11), $H^1(\Omega)$ denotes the standard Sobolev space of square-integrable functions having square-integrable first-order derivatives, Γ is the physical domain boundaries and $\boldsymbol{n}$ the outward normal vector.

3.1.2. *Temporal discretization: finite difference method*

The temporal derivative in the energy and concentration equations is expressed by the finite difference method. First- and second-order backward discretizations are used. The first order is used just for the first time step. The discrete form of the temporal derivative is obtained as follows:

$$\left.\begin{aligned} &\left.\frac{\partial f}{\partial t}\right|_{t=t^n} = \frac{f^n - f^o}{\Delta t^o} + O(\Delta t^r), \\ &f^o = f^{n-1} \quad \text{and} \quad \Delta t^o = \Delta t \qquad \text{when} \quad r = 1, \\ &f^o = \tfrac{4}{3}f^{n-1} - \tfrac{1}{3}f^{n-2} \quad \text{and} \quad \Delta t^o = \tfrac{2}{3}\Delta t \qquad \text{when} \quad r = 2, \end{aligned}\right\} \tag{3.4}$$

where r denotes the scheme order, n, $n-1$ and $n-2$ correspond to t, $t-\Delta t$ and $t-2\Delta t$ respectively and Δt is the time step. The function f stands for θ or φ.

3.1.3. *Spatial discretization: finite element method*

The calculus domain is discretized into rectangular elements known as the nine-noded Lagrangian cubic elements, with non-uniform grid. In each element, the unknown profiles of $\psi(x, y)$, $\theta(x, y)$ and $\varphi(x, y)$ are approximated by

$$\begin{Bmatrix} \psi^e(x,y) \\ \theta^e(x,y) \\ \varphi^e(x,y) \end{Bmatrix} = \sum_{j=1}^{9} \mathcal{N}_j(x,y) \begin{Bmatrix} \psi_j^e \\ \theta_j^e \\ \varphi_j^e \end{Bmatrix}, \tag{3.5}$$

where $\mathcal{N}_j(x, y)$ are the Lagrangian shape functions and ψ_j^e, θ_j^e and φ_j^e the elementary nodal values.

Following the Bubnov Galerkin procedure and using the implicit scheme, the discretized governing equations, after assembling into global systems, are obtained in terms of the following systems of linear equations:

$$\boldsymbol{K}_\psi \boldsymbol{\psi}_k^n = R_T \, \boldsymbol{B} \left(\boldsymbol{\theta}_{k-1}^n - \boldsymbol{\varphi}_{k-1}^n\right), \tag{3.6}$$

$$\left[\frac{1}{\Delta t^o}\boldsymbol{M} - \boldsymbol{C} + \boldsymbol{K}\right]\boldsymbol{\theta}_k^n = \frac{1}{\Delta t^o}\boldsymbol{M}\theta^o + \boldsymbol{L}\boldsymbol{\psi}_k^n, \tag{3.7}$$

$$\left[\frac{\varepsilon}{\Delta t^o}\boldsymbol{M} - \boldsymbol{C} + \frac{1}{Le}\boldsymbol{K}\right]\boldsymbol{\varphi}_k^n = \frac{\varepsilon}{\Delta t^o}\boldsymbol{M}\varphi^o + \boldsymbol{L}\boldsymbol{\psi}_k^n, \tag{3.8}$$

where $\boldsymbol{B}$, $\boldsymbol{C}$, $\boldsymbol{K}_\psi$, $\boldsymbol{K}$, $\boldsymbol{L}$ and $\boldsymbol{M}$ are $m \times m$ global sparse matrices and m is the total node number over the calculus domain ($m = (2N_{ex} + 1)(2N_{ey} + 1)$ where N_{ex} and N_{ey} are the finite element numbers in x- and y-directions). The corresponding elementary

matrices are defined by

$$\left.\begin{aligned} \boldsymbol{B}^e &= \int_{\Omega^e} \frac{\partial \mathcal{N}_j}{\partial x}\mathcal{N}_i \,\mathrm{d}\Omega^e, & \boldsymbol{C}^e &= \int_{\Omega^e} J(\psi_k^n, \mathcal{N}_j)\mathcal{N}_i \,\mathrm{d}\Omega^e, \\ \boldsymbol{K}_\psi^e &= \int_{\Omega^e} \nabla\mathcal{N}_j \cdot \nabla\mathcal{N}_i \,\mathrm{d}\Omega^e, & \boldsymbol{K}^e &= \int_{\Omega^e} \nabla\mathcal{N}_j \cdot \nabla\mathcal{N}_i \,\mathrm{d}\Omega^e, \\ \boldsymbol{L}^e &= -\int_{\Omega^e} \frac{\partial \mathcal{N}_j}{\partial y}\mathcal{N}_i \,\mathrm{d}\Omega^e, & \boldsymbol{M}^e &= \int_{\Omega^e} \mathcal{N}_j\mathcal{N}_i \,\mathrm{d}\Omega^e. \end{aligned}\right\} \tag{3.9}$$

The above integrals are performed using the Gauss integration formulae.

The uncoupling between the momentum equation (3.6) and the energy and species equations (3.7) and (3.8), at a given time step n and iteration k, are obtained by evaluating the temperature and concentration in the buoyancy term of (3.6) and the stream function in the advective terms of (3.7) and (3.8) with the results obtained previously at iteration $k-1$. The convergence of the iterative procedure is obtained when

$$\frac{\sum_i |f_i^k - f_i^{k-1}|}{\sum_i |f_i^k|} \leqslant 10^{-6}, \tag{3.10}$$

where f stand for ψ, θ and φ.

In general, one to three iterations were sufficient to achieve the convergence criteria.

The system of equations (3.6) is solved by the successive over-relaxation method. On the other hand, the systems of equations given by (3.7) and (3.8) are solved by an iterative procedure using the pentadiagonal matrix algorithm (PDMA).

The linear system of equations (3.7) and (3.8) can be reduced to

$$\boldsymbol{E}\boldsymbol{f} = \boldsymbol{Q}, \tag{3.11}$$

where $\boldsymbol{E}$ is the resulting matrix, $\boldsymbol{Q}$ is the right-hand member and $\boldsymbol{f}$ is the unknown vector. With the use of the Lagrangian element, to descritize the computational domain, the resulting matrix $\boldsymbol{E}$ was found to consist of five penta-diagonal matrices. One of these is located on the diagonal of $\boldsymbol{E}$.

The above linear system of equations can be solved by the following iterative procedure:

$$\boldsymbol{PD}\boldsymbol{f}^k = \boldsymbol{PD}\boldsymbol{f}^{k-1} + \zeta(\boldsymbol{Q} - \boldsymbol{E}\boldsymbol{f}^{k-1}), \tag{3.12}$$

where $\boldsymbol{PD}$ is the pentadiagonal matrix of $\boldsymbol{E}$, ζ is the under-relaxation coefficient ($0 < \zeta < 1$) and k denotes iteration k.

The precision of the numerical solution depends on the grid size $N_{ex} \times N_{ey}$, where N_{ex} and N_{ey} are the number of elements in the x- and y-directions respectively. For a square enclosure and typical values of the governing parameters, a grid size varying from 20×20 to 40×40 was sufficient to model accurately the problem. On the other hand, for a slender enclosure, $A \gg 1$, a non-uniform grid size of 20×50 was used. Our numerical results are compared to those obtained by Mamou *et al.* (1995*a*, *b*) and Alavyoon *et al.* (1994) and the error was found to be less than 0.1%. For a slender enclosure of $A = 10$, the numerical results obtained for $R_T = 10$, $Le = 10$ and $\varepsilon = 1$, with a non-uniform (sinusoidal) grid size of 20×60, are $Nu = 1.278$, $Sh = 4.780$ and $\psi_0 = 0.893$, which are in good agreement with the analytical ones $Nu = 1.277$, $Sh = 4.777$ and $\psi_0 = 0.892$. Grid refinement tests indicated that heat and mass transfer rates and stream function values were within 0.5%. For $R_T = 50$, $Le = 10$, $\varepsilon = 1$ and $A = 4$ with a grid size of 15×30 and time step $\Delta t = 10^{-4}$, the

CPU time required to achieve a maximal dimensionless time $t = 5$ was about 37.5 hours on a RISC6000 work station.

3.2. *Analytical solution: parallel flow approximation*

In this section, an analytical solution for the finite-amplitude convection within a porous cavity is proposed. In the limit of slender enclosures, $A \gg 1$, the governing equations can be considerably simplified and solved analytically using the parallel flow approximation in which $u(x, y) \simeq 0$ and $v(x, y) \simeq v(x)$ in the central part of the enclosure. For this situation, it can be demonstrated that the temperature and concentration are linearly stratified in the vertical direction (see, for instance, Alavyoon 1993 and Mamou *et al.* 1995*b*). With these approximations, the governing equations (2.7)–(2.9), can be reduced to a set of ordinary differential equations that can be easily solved to yield the stream function, temperature and concentration distributions as

$$\left.\begin{aligned} \psi(x, y) &= \psi_0 \cos \omega x, \\ \theta(x, y) &= C_T\ y - \frac{\psi_0}{\omega} C_T \sin \omega x, \\ \varphi(x, y) &= C_S\ y - \frac{\psi_0}{\omega} LeC_S \sin \omega x, \end{aligned}\right\} \tag{3.13}$$

where ψ_0 is the stream function value at the centre of the enclosure, C_T and C_S are unknown constant temperature and concentration gradients in the y-direction respectively and

$$\omega = [R_T(LeC_S - C_T)]^{1/2}. \tag{3.14}$$

From the stream function boundary condition, (2.11), it follows that

$$\psi_0 \cos(\omega/2) = 0. \tag{3.15}$$

According to the above relation, the motionless diffusive solution (i.e. $\psi = \theta = \varphi = 0$) is a possible solution. This solution is expected to be stable up to a subcritical Rayleigh number, R_{TC}^{sub}, above which a convective motion bifurcates from the rest state. Hence, the convective flow solution can be deduced from (3.15) such that

$$\omega = (2\ell + 1)\pi, \qquad \ell = 0, 1, 2 \ldots. \tag{3.16}$$

In the above relation, ℓ corresponds to different convective modes. Thus, for $\ell = 0$, the flow structure is unicellular and for $\ell \geqslant 1$ the flow structure consists of $(2\ell + 1)$ vertical cells. For the unicellular mode ($\ell = 0$), it was demonstrated by Alavyoon *et al.* (1994) that when the buoyancy ratio N approaches -1, the parameter ω tends towards the constant value π. This result is predicted by the present solution, (3.16), when $\ell = 0$.

The energy and species balances at each transversal section of the enclosure yields (see, for instance, Mamou, Vasseur & Bilgen 1996)

$$C_T = 4(-1)^{\ell} \frac{\psi_0}{\omega(\psi_0^2 + 2)}, \qquad C_S = 4\ (-1)^{\ell} \frac{Le\ \psi_0}{\omega(Le^2\psi_0^2 + 2)}. \tag{3.17}$$

Upon combining (3.14) and (3.17), it is readily found that

$$a^2Le^2\ \psi_0^4 + a(Le^2 + 1)\ \psi_0^2 - 2a^{1/2}(-1)^{\ell}(Le^2 - 1)R_T^0\ \psi_0 + 1 = 0, \tag{3.18}$$

where $a = 0.5$ and R_T^0 is defined as

$$R_T^0 = \frac{R_T}{R^{sub}} \quad \text{with} \quad R^{sub} = \frac{\omega^3}{2a^{1/2}}. \tag{3.19}$$

In general, for given values of R_T and Le, ψ_0 can be computed numerically using, for example, the Newton–Raphson method.

From the above results, the critical Rayleigh number R_{TC}^{sub}, for the onset of motion, can be derived in terms of the Lewis number, Le. Putting the derivative of ψ_0 with respect to R_T into (3.18) and setting the resulting expression equal to infinity, it is readily found that

$$R_{TC}^{sub} = R^{sub}\frac{(-1)^{\ell}a^{1/2}}{(Le^2-1)}[2aLe^2\psi_{0C}^3 + (Le^2+1)\psi_{0C}], \tag{3.20}$$

where ψ_{0C} is the critical stream function value located at the centre of the enclosure which can be computed from

$$\psi_{0C} = \pm\frac{1}{Le(6a)^{1/2}}[((Le^2+1)^2 + 12Le^2)^{1/2} - (Le^2+1)]^{1/2}. \tag{3.21}$$

According to (3.20), the lowest critical Rayleigh number at which thermosolutal convection exists is given by the unicellular motion (i.e. $\ell = 0$). For this particular mode, the convective cell is clockwise when $Le < 1$, but counterclockwise when $Le > 1$. For $\ell = 1$, the flow structure consists of three identical counter-rotating convective cells. When $Le > 1$, the central convective cell is clockwise and the two side cells are counterclockwise, and vice versa when $Le < 1$.

For large or small Lewis numbers, the subcritical Rayleigh number expression, (3.20), reduces to

$$R_{TC}^{sub} = \frac{R^{sub}}{(1-Le)}, \tag{3.22}$$

where R^{sub} is a constant having the following values:

$$\left.\begin{aligned} R^{sub} &= \frac{\omega^3}{\sqrt{2}} \quad \text{when} \quad Le \ll 1, \\ R^{sub} &= -\frac{\omega^3}{\sqrt{2}} \quad \text{when} \quad Le \gg 1. \end{aligned}\right\} \tag{3.23}$$

The Nusselt and Sherwood numbers, which are of interest in engineering applications, are given by (2.15), which in view of (2.5) and (3.13) reduce to

$$Nu = \frac{\omega^2\psi_0^2 + 2\omega^2}{(\omega^2-8)\psi_0^2 + 2\omega^2}, \qquad Sh = \frac{\omega^2Le^2\psi_0^2 + 2\omega^2}{(\omega^2-8)Le^2\psi_0^2 + 2\omega^2}. \tag{3.24}$$

3.3. *Results and discussion*

Figures 2 and 3 exemplify the effects of the thermal Rayleigh number, R_T, and the Lewis number, Le, on the flow intensity (ψ_0), and heat and mass transfer rates (Nu and Sh). For a given set of the governing parameters, such that convective motion is possible, the parallel flow approximation predicts the existence of two different convective solutions bifurcating from the rest state. The solution corresponding to the higher convective mode, represented in the graphs by solid lines, was found to be stable and in good agreement with the numerical one depicted by solid circles.

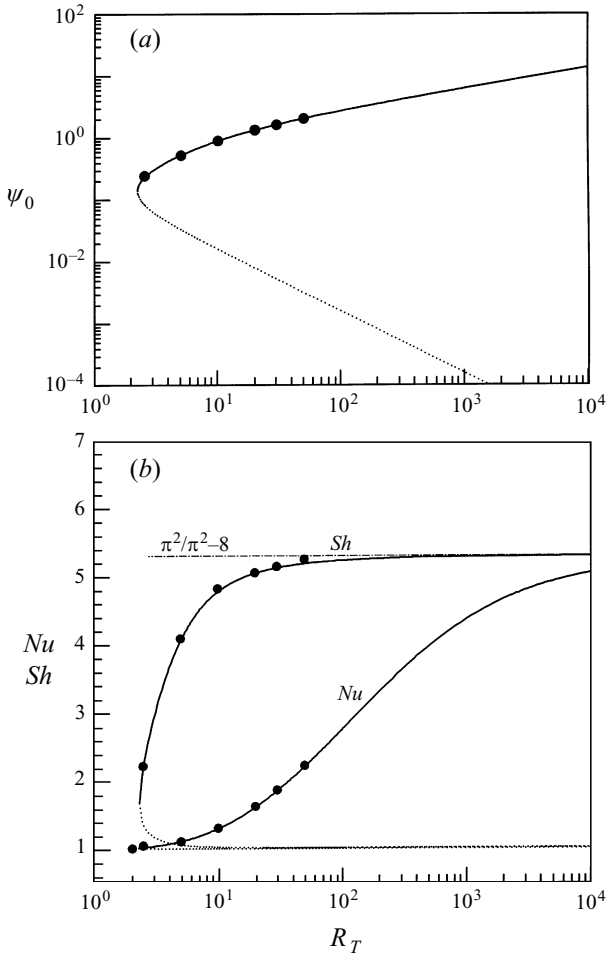

FIGURE 2. Comparison between the numerical (circles) and the analytical solutions for $Le = 10$: (a) stream function at the centre of the cavity versus R_T and (b) Nusselt and Sherwood numbers versus R_T.

However, it has not been possible to confirm numerically the existence of the lower convective mode solution, shown as dotted lines. Hereafter, the former will be referred as the 'stable branch' of the solution and the latter as the 'unstable branch'. All the numerical results presented in these figures were obtained for a cavity having an aspect ratio, A, ranging from 4 to 10 and for a normalized porosity of $\varepsilon = 0.9$.

Figures 2(a) and 2(b) illustrate how the convective flow intensity, and the heat and mass transfer rates vary with R_T, when $Le = 10$. According to the analytical solution, for a given Le, there exists a subcritical Rayleigh number R_{TC}^{sub} for the onset of convection. As will be demonstrated later on, this Rayleigh number is below the supercritical one, R_{TC}^{sup}, predicted by the linear stability theory. From (3.20), it is found that $R_{TC}^{sub} = 2.236$ when $Le = 10$. The onset of motion, as shown in the graphs, is characterized by a finite-amplitude convective motion ($\psi_0 = 0.139$) such that the mass transfer rate ($Sh = 1.660$) and to a less extent the heat transfer rate ($Nu = 1.008$), are due to convection. For values of R_T above the critical value, the unstable branch indicates that the solution approaches asymptotically the conductive

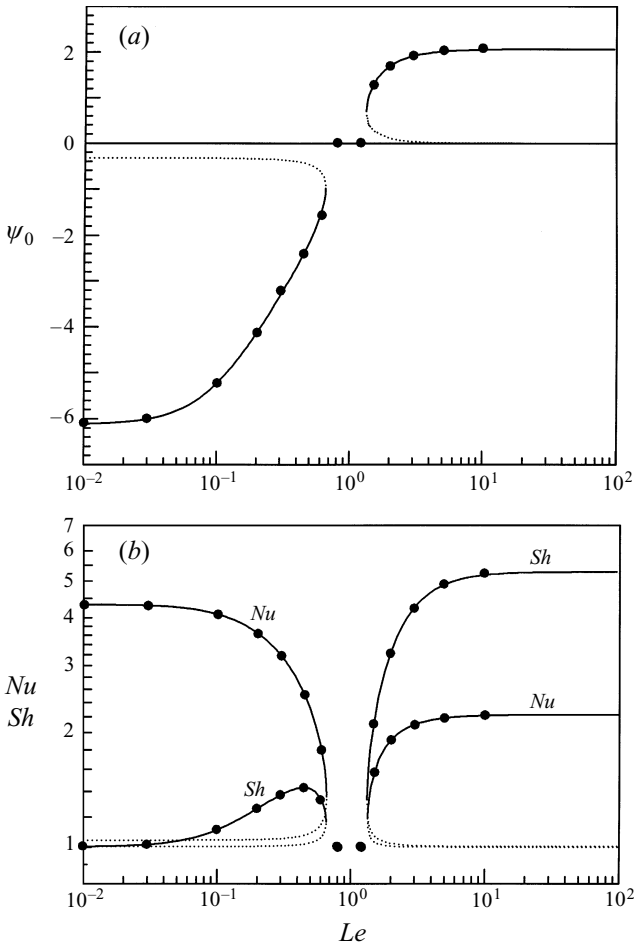

FIGURE 3. Comparison between the numerical and the analytical solutions for $R_T = 50$: (*a*) stream function at the centre of the cavity versus *Le* and (*b*) Nusselt and Sherwood numbers versus *Le*.

regime. On the other hand, the stable branch shows that ψ_0, Nu and Sh increase first with R_T. Then, for larger values of R_T, the flow intensity continues to increase monotonically with R_T according to $\psi_0 = (2/\pi)R_T^{1/3}$. However, both Nu and Sh are observed to reach asymptotically a constant value ($Nu = Sh = \pi^2/(\pi^2 - 8) \simeq 5.239$). This behaviour results from the imposition of constant heat and mass fluxes on the vertical boundaries. A similar trend has been reported by Vasseur, Robillard & Sen (1989) while considering the case of a horizontal porous layer, saturated with a pure fluid, heated from below by a constant heat flux. For ordinary values of R_T such that $R_T \leqslant 70$ when $Le = 10$, a good agreement is observed between the numerical and analytical results. However, when R_T is made very large ($R_T \geqslant 100$), a steady or oscillatory numerical solution bifurcates from the analytical one (Hopf's bifurcation). This point will be discussed later on.

The variations of the flow intensity and the heat and mass transfer rates with *Le* are illustrated in figures 3(*a*) and 3(*b*), for $R_T = 50$. The results indicate that for $0.659 \leqslant Le \leqslant 1.339$, a purely diffusive (motionless) regime prevails since, for this range of *Le*, $R_T = 50$ is below the subcritical Rayleigh number, R_{TC}^{sub} (3.20), for

the onset of convective motion. The effect of decreasing Le below unity, for which the faster diffusing component is the solute, will be discussed first. At $Le = 0.659$, the transition from the conductive regime to a steady convective regime is through finite-amplitude instability ($\psi_0 = -0.984$, $Nu = 1.360$ and $Sh = 1.164$). As the value of Le is made smaller, figure 3(a) indicates that the strength of the convective motion increases progressively up to a constant value. This trend is due to the fact that, when $Le \to 0$, the only way for the mass to be transferred is by conduction. So the buoyancy force remains unaffected when Le becomes smaller and smaller. As depicted by figure 3(b), the Sherwood number, on the other hand, is observed first to pass through a maximum and then to decrease asymptotically towards unity. This situation, for which the concentration distribution is linear ($S = x$), does not correspond to a purely diffusive (motionless) regime as observed when $0.659 \leqslant Le \leqslant 1.339$. Rather, it is a consequence of the fact that, when $Le \ll 1$, the mass diffusivity, D, is much higher than the thermal one, α. Indeed, this linear concentration distribution gives a maximum flow intensity, as indicated by the value of ψ_0. As the value of Le is made large enough, the convective flow intensity and the heat and mass transfer rates become independent of the Lewis number. As can be observed from the graphs, when $Le < 1$, the lower diffusive component is the heat, as a result the heat transfer is due mainly to convection ($Nu > Sh$). However, when $Le > 1$, the faster diffusive component is heat and the solute transfer is dominated by convection ($Sh > Nu$).

As can be seen from figure 3(a), when Le varies from 10^{-2} to 10^2, a transition of the flow circulation from clockwise to counterclockwise directions occurs. The analytical solution indicates that the circulation is clockwise ($\psi_0 < 0$) when $Le < 1$ and counterclockwise ($\psi_0 > 0$) when $Le > 1$. To explain the effect of Le on the flow circulation direction, consider the case of $Le < 1$. Recall that, in a vertical enclosure, the buoyancy force is governed solely by horizontal thermal and solutal gradients. Since the solute diffuses more quickly than heat ($Le < 1$), the horizontal mass gradient is greater than the thermal one. For this case, the mass effects are predominant giving rise to a clockwise flow circulation. For the same reason, when $Le > 1$ the flow circulation is counterclockwise.

For a square enclosure, the numerical results (not presented here) showed the existence of a subcritical convection. After some numerical runs for $\varepsilon = 1$ and different values of R_T and Le, the flow intensity, ψ_0, and the subcritical Rayleigh number expressions were found to be similar to that obtained analytically for a slender enclosure (see (3.18) and (3.20)). For instance, for $A = 1$, the values of a and R^{sub} were determined numerically and found to be independent of R_T and Le around the bifurcation point. They are given approximately by

$$a = 0.312, \quad R^{sub} = 46.51, \tag{3.25}$$

as compared with the analytical values $a = 0.5$ and $R^{sub} = \pi^3/\sqrt{2}$ predicted for $A \to \infty$.

One of the most important characteristics of double-diffusive convection is the possible occurrence of oscillatory flows when the buoyancy forces oppose each other. Recently, this phenomenon has been demonstrated numerically by Alavyoon *et al.* (1994) who found that for $\varepsilon = 1$ and sufficiently large numbers R_T, Le and A, oscillating flows are possible when the temperature and solute concentration gradients are opposing each other and of comparable magnitude.

In the present investigation, the effect of ε on the final converged convective solution has been studied (see figure 4). Depending on the values of ε, the convective solution can be stationary or oscillatory for a given set of the other governing parameters.

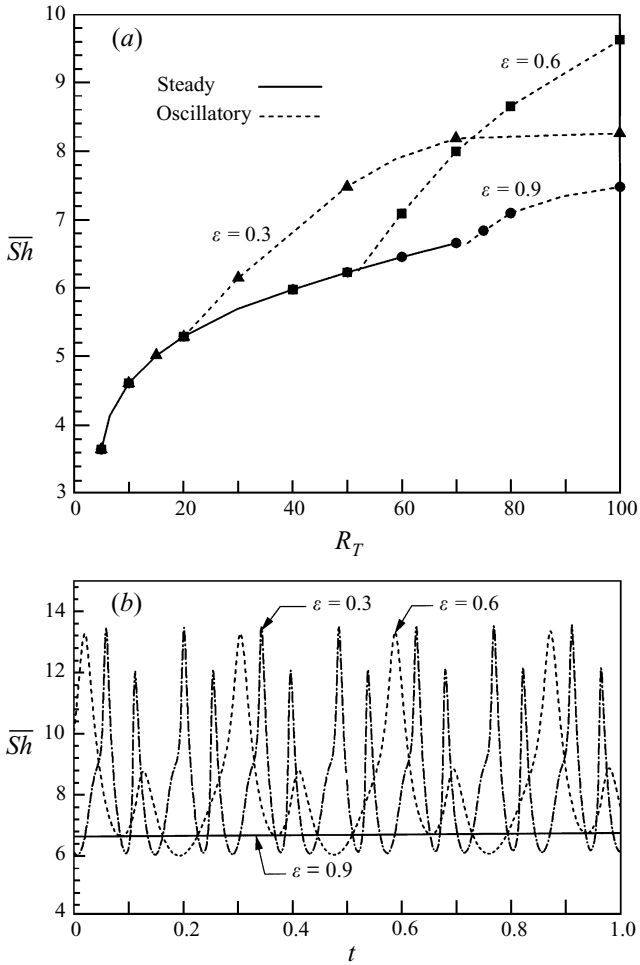

FIGURE 4. (*a*) Average Sherwood number versus R_T for $Le = 10$, $A = 4$ and $\varepsilon = 0.3$, 0.6 and 0.9, (*b*) average Sherwood number versus t for $R_T = 70$, $Le = 10$, $A = 4$ and $\varepsilon = 0.3$, 0.6 and 0.9.

Figure 4(*a*) illustrates the effect of R_T on the average Sherwood number, $\overline{Sh}$, on the vertical walls obtained for $Le = 10$ and $A = 4$. The steady state solution is illustrated with solid line and the periodic oscillatory ones by dashed lines. In the oscillating regime, the mean value of $\overline{Sh}$ over a time period, τ, was used to determine a point of the curve. The intersection between the solid and dashed lines indicates approximately the critical Rayleigh number, R_T^{ε}, at which the transition from the convective steady state to the oscillatory convective regimes occurs. By extrapolation, it was found that $R_T^{\varepsilon} \simeq 20$, 52 and 72 when $\varepsilon = 0.3$, 0.6 and 0.9, respectively. It follows that the critical Rayleigh number, R_T^{ε}, for a Hopf bifurcation depends strongly on the normalized porosity, ε, of the porous medium. The time history of $\overline{Sh}$ is exemplified in figure 4(*b*) for $R_T = 70$, $Le = 10$ and $A = 4$ and $\varepsilon = 0.3$, 0.6 and 0.9. As can be seen from the graph, the behaviour of the converged convective solution shows a strong dependence on the normalized porosity, ε. The convective flow was observed to be steady when $\varepsilon = 0.9$, whereas for $\varepsilon = 0.3$ and 0.6 it was found to oscillate periodically. For the oscillatory convective regime, the oscillation frequency f_r ($f_r = 1/\tau$) was observed to depend on the value of ε. It was found numerically that $f_r = 3.53$ when $\varepsilon = 0.6$

and $f_r = 7.05$ when $\varepsilon = 0.3$. The latter is two times greater than the former, which demonstrates clearly that when the normalized porosity tends towards small values, the frequency tends towards large values so the convective flow becomes more and more unstable and oscillates.

4. Linear stability analysis

The linear stability of the basic rest state solution, (2.6), in terms of the governing parameters of the problem, is now considered.

Assuming separability, the dynamic perturbation ($\psi(x, y)$, $\theta(x, y)$, $\varphi(x, y)$), (2.5), is written as follows:

$$\left.\begin{aligned} \psi(t, x, y) &= \psi_0 \, \mathrm{e}^{pt} \, F(x, y), \\ \theta(t, x, y) &= \theta_0 \, \mathrm{e}^{pt} \, G(x, y), \\ \varphi(t, x, y) &= \varphi_0 \, \mathrm{e}^{pt} \, G(x, y), \end{aligned}\right\} \tag{4.1}$$

where $F(x, y)$ and $G(x, y)$ are unknown space functions satisfying the boundary conditions given by (2.11) (substitute ψ by F and θ and φ by G). They describe the perturbed stream function $\psi(x, y)$, temperature $\theta(x, y)$ and concentration $\varphi(x, y)$ fields at the onset of convection; ψ_0, θ_0 and φ_0 are constants and p is the growing rate of the perturbation amplitude.

Substituting (4.1) into (2.7)–(2.9) and neglecting the second-order nonlinear terms, it is readily found that

$$\left.\begin{aligned} \psi_0 \, \nabla^2 F &= -R_T \, (\theta_0 - \varphi_0) \, \frac{\partial G}{\partial x}, \\ p \, \theta_0 \, G + \psi_0 \, \frac{\partial F}{\partial y} &= \theta_0 \, \nabla^2 G, \\ p \, \varepsilon \, \varphi_0 \, G + \psi_0 \, \frac{\partial F}{\partial y} &= \frac{\varphi_0}{Le} \, \nabla^2 G. \end{aligned}\right\} \tag{4.2}$$

The conditions for stationary and oscillatory instabilities will be now discussed in turn.

In the foregoing sections, a finite element method is used to solve the above linear system of equations to obtain the supercritical Rayleigh number and the corresponding stream function, temperature and concentration fields at the onset of supercritical convection. These results will be used together with the Galerkin method to examine the possible occurrence of oscillatory modes of instability.

4.1. *Instability via stationary convection: $p = 0$*

The marginal state of stability via stationary convection, for which the exchange of stability is valid, can be deduced from (4.2) when the value of p is made equal to zero. The resulting set of equations can be solved numerically using the finite element method (see § 3.1). Hence, the discretized equations are obtained as follows:

$$\psi_0 \, \boldsymbol{K}_{\psi} \boldsymbol{F} = R_T \, (\theta_0 - \varphi_0) \, \boldsymbol{B} \boldsymbol{G}, \tag{4.3}$$

$$\psi_0 \, \boldsymbol{L} \boldsymbol{F} = \theta_0 \, \boldsymbol{K} \boldsymbol{G}, \tag{4.4}$$

$$\psi_0 \, \boldsymbol{L} \boldsymbol{F} = \frac{\varphi_0}{Le} \, \boldsymbol{K} \boldsymbol{G}, \tag{4.5}$$

where $\boldsymbol{B}$, $\boldsymbol{K}_\psi$, $\boldsymbol{K}$ and $\boldsymbol{L}$ are $m \times m$ square matrices. They are defined in (3.9). It is noted that, upon considering the boundary conditions (2.11), the matrices $\boldsymbol{K}_\psi$ and $\boldsymbol{K}$ become different from each other. The Dirichlet boundary conditions are introduced in the above systems of equations without altering the size of the matrices (see, for instance, Huebner, Thornton & Byrom 1995). In (4.3), if i is the subscript of a known nodal value of F on the boundaries ($F = 0$) the ith row and the ith column of $\boldsymbol{K}_\psi$ are set equal to zero and the diagonal element, $\boldsymbol{K}_{\psi i,i}$, is set equal to unity. On the other hand, the ith row of $\boldsymbol{B}$ is set equal to zero. The thermal and solutal boundary conditions, (2.11), are introduced in (4.4) and (4.5) by using the same technique.

From (4.4) and (4.5) it can be observed that $\varphi_0 = Le\ \theta_0$. Thus upon combining the linear systems, (4.3)–(4.5), one can obtain the following canonical eigenvalue problem:

$$[\boldsymbol{E} - \lambda \boldsymbol{I}]\, \boldsymbol{F} = 0, \tag{4.6}$$

where $\boldsymbol{E}$ is an $m \times m$ square matrix defined as $\boldsymbol{E} = \boldsymbol{K}_\psi^{-1}\boldsymbol{B}\boldsymbol{K}^{-1}\boldsymbol{L}$, $\boldsymbol{I}$ is the identity matrix, $\boldsymbol{F}$ is the unknown eigenvector and λ is the eigenvalue defined such that

$$R_T(1 - Le) = \frac{1}{\lambda}. \tag{4.7}$$

From the mathematical point of view, a non-trivial solution ($\boldsymbol{F} \neq 0$) to (4.6) exists if and only if the determinant of $[\boldsymbol{E} - \lambda \boldsymbol{I}]$ is zero. This permits us to determine all eigenvalues of the matrix $\boldsymbol{E}$. Using double-precision subroutines of the IMSL library, the solution of (4.6) yields m eigenvalues, λ_i, with their corresponding eigenvectors, $\boldsymbol{F}_i$, where $i = 1, m$.

If the eigenvalues can be rearranged as

$$\lambda_1 \leqslant \lambda_2 \leqslant \ldots\ldots \leqslant \lambda_{m-1} \leqslant \lambda_m \tag{4.8}$$

then the supercritical Rayleigh number for the onset of motion is given by

$$R_{TC}^{sup} = \frac{R^{sup}}{(1 - Le)} \tag{4.9}$$

where R^{sup} is a constant depending on the aspect ratio, A, of the cavity. It is given by

$$\left.\begin{aligned} R^{sup} &= \frac{1}{\lambda_1} \quad \text{when} \quad Le > 1, \\ R^{sup} &= \frac{1}{\lambda_m} \quad \text{when} \quad Le < 1. \end{aligned}\right\} \tag{4.10}$$

Hence, the stream function field at the onset of convection is given by

$$\left.\begin{aligned} &\pm\boldsymbol{F}_1 \quad \text{when} \quad Le > 1, \\ &\pm\boldsymbol{F}_m \quad \text{when} \quad Le < 1. \end{aligned}\right\} \tag{4.11}$$

From (4.4) and (4.5), the temperature and concentration fields $\boldsymbol{G}$ are then obtained from

$$\boldsymbol{G}_i = \frac{\psi_0}{\theta_0}\, \boldsymbol{K}^{-1}\boldsymbol{L}\boldsymbol{F}_i. \tag{4.12}$$

4.1.1. *Validation*

Recently, the critical Rayleigh number for the onset of motion in a horizontal layer heated from below by a constant heat flux, has been predicted analytically by Kimura, Vynnycky & Alavyoon (1995) as a function of the aspect ratio of the

$N_{ex} \times N_{ey}$	4×4	8×8	12×12	Kimura *et al.* (1995)
R^{sup}	22.975 248	22.947 851	22.946 282	22.945 889
Error (%)	1.28×10^{-1}	8.55×10^{-3}	1.71×10^{-3}	
CPU (s)	1.13	36.38	488.76	

TABLE 1. Effect of the grid size on the precision of the computed value of R^{sup} for a square enclosure ($A = 1$) heated from below by a constant heat flux.

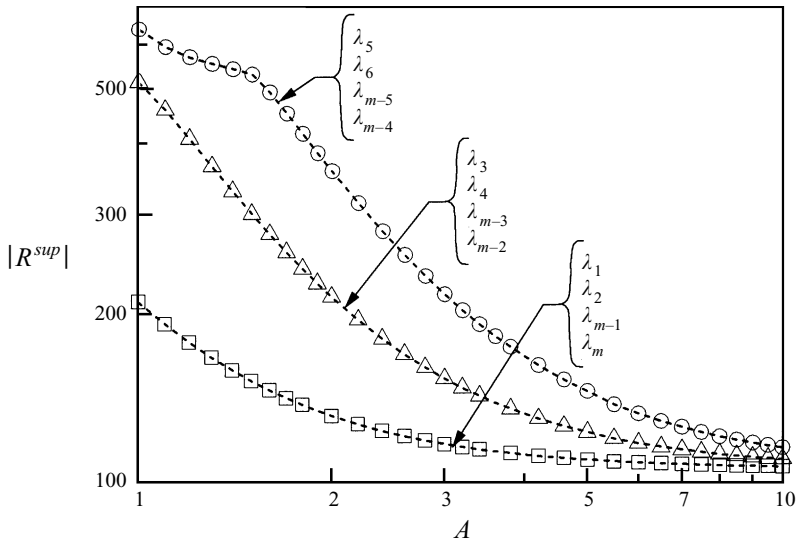

FIGURE 5. Critical value of R^{sup} versus A.

enclosure A. Their results are considered here for validation. The precision of the value of R^{sup}, predicted by the present finite element method, was found to depend naturally on the grid numbers ($N_{ex} \times N_{ey}$) in the numerical domain. To determine the best compromise between the accuracy of the results and the computing time, numerical tests were carried out for a square enclosure using various mesh sizes. Typical results are presented in table 1 and they are in good agreement with the analytical results. For an aspect ratio of $A = 100$, it is found with the present numerical solution that, for a grid size of 10×20, $R^{sup} = 12.001\,130$. This is in good agreement with the analytical value $R^{sup} = 12.001\,128$ predicted by Kimura *et al.* (1995) and the value $R^{sup} = 12$ reported by Nield (1968) for the case of an infinite layer ($A \to \infty$). One can observe that the deviation of our numerical results from the analytical one is about 16.5×10^{-6} %. According to the above tests, a mesh size of 10×10 for $A = 1$ is sufficient to model accurately the problem. However, a mesh size of 10×40 is required for $A = 10$, especially when the flow structure is multicellular.

4.1.2. *Results and discussion*

For a vertical enclosure, typical results obtained with the numerical procedure described above will be now discussed. The numerically determined constant R^{sup} is presented in figure 5 as a function of the aspect ratio A. For a given A, four solutions

i	$\lambda_i \times 10^3$	$R_i^{sup} = 1/\lambda_i$
1	−4.7656	−209.8360
2	−4.7656	−209.8360
3	−1.9614	−509.8315
4	−1.9614	−509.8316
.....	.....	.....
1761	1.9614	509.8316
1762	1.9614	509.8315
1763	4.7651	209.8360
1764	4.7651	209.8360

TABLE 2. Computed eigenvalues λ_i and constants R_i^{sup} for a square enclosure ($A = 1$) with grid size of 20×20 elements (node number is $m = 1764$).

corresponding to the existence of four eigenvalues are possible with the same absolute value but a different sign. It was found that $\lambda_i = \lambda_{i+1}$, $i = 1, 3, 5, \ldots, m-1$, for which the corresponding flow structures $\boldsymbol{F}_i$ and $\boldsymbol{F}_{i+1}$ are different from each other, and $\lambda_i = -\lambda_{m-i+1}$ for which $\boldsymbol{F}_i$ and $\boldsymbol{F}_{m-i+1}$ are the mirror images of each other. Typical results obtained for $A = 1$ are presented in table 2. The minimum and maximum eigenvalues give the supercritical Rayleigh numbers for the onset of convection when $Le > 1$ and $Le < 1$ respectively. Numerical results show that R^{sup} is positive when $Le < 1$ and negative when $Le > 1$. For this reason, the curve in figure 5 is presented in terms of the absolute value of R^{sup}. As expected, the results indicate that the value of R^{sup} decreases monotonically as the value of A is made larger. When A is sufficiently large, say, $A \geqslant 10$ the infinite vertical layer limit is approximately achieved.

Figures 6 and 7 present the streamlines, isotherm and isoconcentration patterns of the perturbation solution (ψ, θ and ϕ), at the onset of supercritical convection, for $A = 1$, 5 and ∞. As discussed above, for a given value of the aspect ratio, A, and $Le > 1$, the computation indicates the existence of double roots of the eigenvalues ($\lambda_i = \lambda_{i+1}$, $i = 1, 3, 5, \ldots, m-1$) and the corresponding eigenvector $\boldsymbol{F}_i$ consisting of two different flow patterns. Thus, for $A = 1$, figure 6(*a*) shows that the first flow pattern obtained for λ_1 consists of two cells of equal size, a thermally (solutal) driven counterclockwise (clockwise) rotating cell in the upper part of the cavity and a solutal (thermally) driven clockwise (counterclockwise) circulation in the lower part of the cavity. The second flow pattern corresponding to λ_2 (see figure 6*b*) consists of a primary solutal (thermally) driven clockwise (counterclockwise) cell rising up (sinking down) at the left-hand wall and sinking (rising up) along the left-hand side. The presence of two secondary thermally (solutably) driven counterclockwise (clockwise) circulation is also observed. The critical Rayleigh number for the onset of supercritical convection, corresponding to these two flow patterns, was found to be $R_{TC}^{sup}(1 - Le) = R^{sup}$ where $R^{sup} = \pm 209.86$ for $A = 1$. Upon increasing A from 1 to 5, the numerical results reveal the formation of multilayered counter-rotating roll cells. The number of cells was found to increase progressively with A. The results obtained for $A = 5$ are presented in figures 6(*e*) and 6(*f*) for $Le > 1$. The flow structure corresponding to λ_1 (or λ_2) consists of five (or six) roll cells and the corresponding critical value is $R^{sup} = \pm 109.74$. For $Le < 1$, the solution is seen to be a mirror image of that corresponding to $Le > 1$ (compare, for instance, figures 6*a* with 6*c*, 6*b* with 6*d*, 6*e* with 6*g* and 6*f* with 6*h*).

For the case of an infinite vertical porous layer $A \to \infty$, the solution shows the

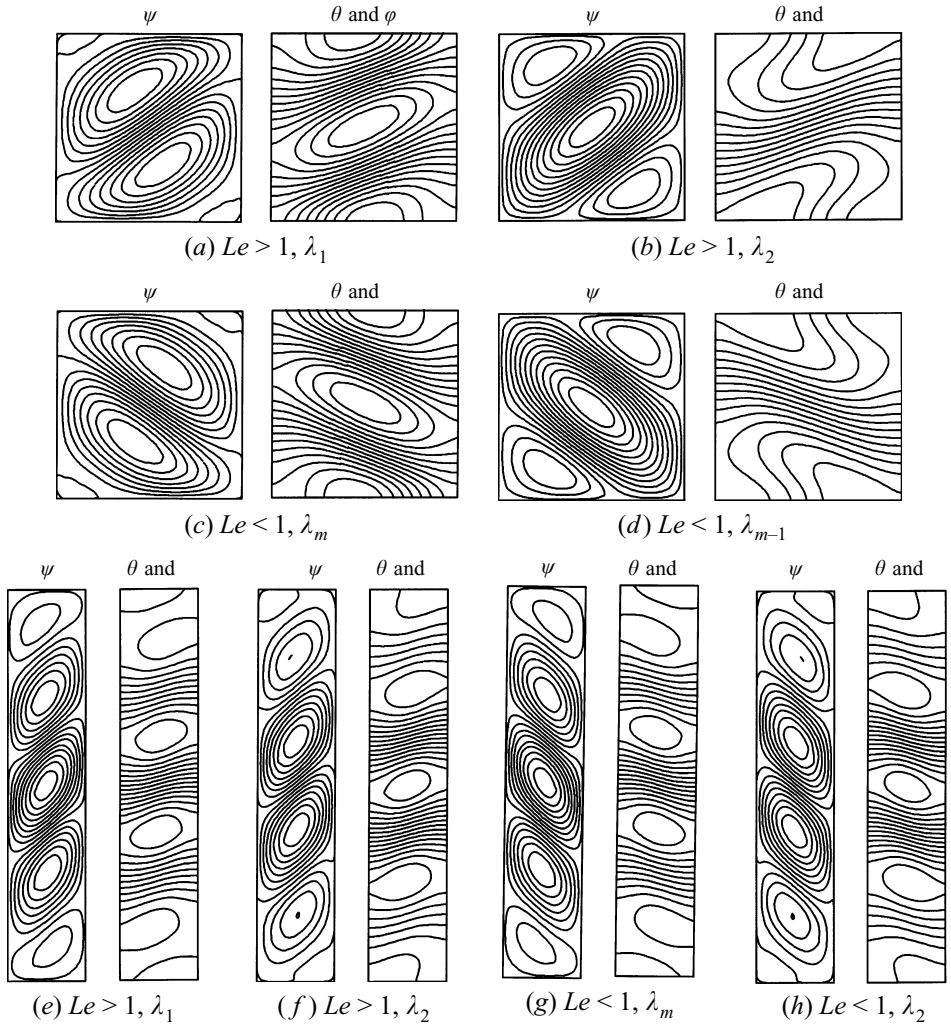

FIGURE 6. Numerical results for the onset of convection as predicted by the linear stability analysis: streamlines, isotherms and isoconcentrations patterns for $A = 1$: (*a*) $R^{sup} = -209.836$, (*b*) $R^{sup} = -209.836$, (*c*) $R^{sup} = 209.836$, (*d*) $R^{sup} = 209.836$, and for $A = 5$: (*e*) $R^{sup} = -109.574$, (*f*) $R^{sup} = -109.574$, (*g*) $R^{sup} = 109.574$, (*h*) $R^{sup} = 109.574$.

formation of a periodic flow structure consisting of tilted counter-rotating roll cells in the y-direction. Consequently, the domain to be solved numerically was restricted to a rectangular channel with periodic boundary conditions applied on the top and bottom horizontal boundaries such that $f(x, y) = f(x, y + A_C)$, where f stands for ψ, θ and φ and A_C is the wavenumber. In this way, R^{sup} was obtained for various values of A in figure 7*a*. Hence, the minimum of R^{sup} corresponds to the critical Rayleigh number for the onset of convection in an infinite vertical layer. In this way it was found that $R^{sup} = \pm 105.335$ and $A_C = 2.504$. The corresponding streamline, isotherm and concentration for an infinite vertical layer are depicted in figure 7(*b*, *c*). For this situation, the flow patterns corresponding to λ_1 and λ_2 or to λ_m and λ_{m-1} were found to be identical.

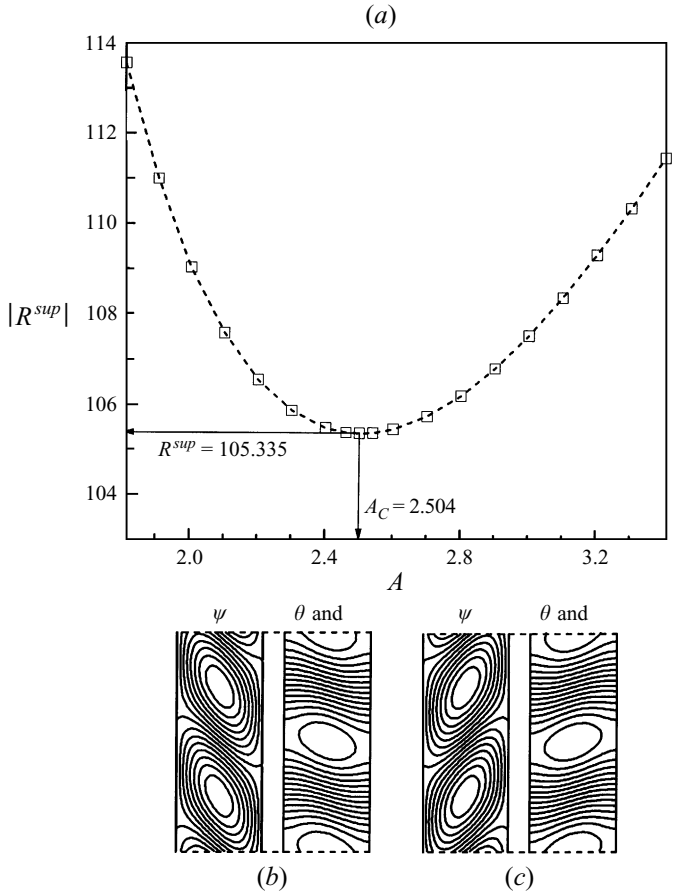

FIGURE 7. Numerical results for the onset of convection as predicted by the linear stability analysis: (*a*) R^{sup} versus A with periodic boundary conditions, streamlines, isotherms and isoconcentrations patterns for $A = 2.504$; (*b*) λ_m, $R^{sup} = 105.335$, (*c*) λ_1, $R^{sup} = -105.335$.

4.2. *Instability via oscillatory convection ($p \neq 0$)*

The linear transient problem stated in (4.2) is solved with the weighted residual method in which $F(x, y)$ and $G(x, y)$ are used as weighted functions. This method has also been used by Mamou (1998) to study oscillatory convection instability in an inclined porous enclosure subject to different boundary condition. Following the Galerkin procedure, one can obtain the following linear equations:

$$\mathscr{K}_{\psi}\ \psi_0 = R_T\ \mathscr{B}\ (\theta_0 - \varphi_0), \tag{4.13}$$

$$p\ \mathscr{M}\ \theta_0 - \mathscr{L}\psi_0 = -\mathscr{K}\ \theta_0, \tag{4.14}$$

$$\varepsilon\ \mathscr{M}\ p\ \varphi_0 - \mathscr{L}\ \psi_0 = -\frac{\mathscr{K}}{Le}\ \varphi_0, \tag{4.15}$$

where $\mathscr{B}$, $\mathscr{K}_{\psi}$, $\mathscr{K}$, $\mathscr{L}$, and $\mathscr{M}$ are constants which can be expressed in terms of the

following integrals:

$$\left.\begin{aligned} \mathscr{B} &= \int_\Omega \frac{\partial G}{\partial x} F \, \mathrm{d}\Omega, \quad \mathscr{L} = -\int_\Omega \frac{\partial F}{\partial y} \, G \, \mathrm{d}\Omega, \\ \mathscr{K}_\psi &= \int_\Omega (\nabla F)^2 \, \mathrm{d}\Omega, \quad \mathscr{K} = \int_\Omega (\nabla G)^2 \, \mathrm{d}\Omega, \quad \mathscr{M} = \int_\Omega G^2 \, \mathrm{d}\Omega. \end{aligned}\right\} \tag{4.16}$$

One can note that the fields of the functions $F(x, y)$ and $G(x, y)$ are obtained numerically from (4.11) and (4.12). Thus, the above integrals can be computed numerically by the finite element method which yields the following expressions:

$$\left.\begin{aligned} \mathscr{B} &= \sum_{k=1}^{N^e} \left(\sum_{i=1}^{9} \sum_{j=1}^{9} \boldsymbol{B}^e_{i,j} \; \boldsymbol{G}^e_j \boldsymbol{F}^e_i \right)_k, \quad \mathscr{L} = \sum_{k=1}^{N^e} \left(\sum_{i=1}^{9} \sum_{j=1}^{9} \boldsymbol{L}^e_{i,j} \; \boldsymbol{F}^e_j \boldsymbol{G}^e_i \right)_k, \\ \mathscr{K}_\psi &= \sum_{k=1}^{N^e} \left(\sum_{i=1}^{9} \sum_{j=1}^{9} \boldsymbol{K}_{\psi \; i,j}^{\;e} \boldsymbol{F}^e_j \boldsymbol{F}^e_i \right)_k, \quad \mathscr{K} = \sum_{k=1}^{N^e} \left(\sum_{i=1}^{9} \sum_{j=1}^{9} \boldsymbol{K}^e_{i,j} \boldsymbol{G}^e_j \boldsymbol{G}^e_i \right)_k, \\ \mathscr{M} &= \sum_{k=1}^{N^e} \left(\sum_{i=1}^{9} \sum_{j=1}^{9} \boldsymbol{M}^e_{i,j} \; \boldsymbol{G}^e_j \boldsymbol{G}^e_i \right)_k, \end{aligned}\right\} \tag{4.17}$$

where N^e is the total number of elements over the computational domain and the superscript e refers to a finite element in the discretized domain.

Substituting (4.14) and (4.15) into (4.13) yields a second-order polynomial equation in term of the growth rate p

$$p^2 - 2p_0 p_1 \; p - p_0^2 p_2 = 0, \tag{4.18}$$

where

$$\left.\begin{aligned} p_0 &= \frac{\gamma}{2\varepsilon Le R^{sup}}, \quad p_1 = R_T Le(\varepsilon - 1) - R^{sup}(1 + \varepsilon Le), \\ p_2 &= 4R^{sup} \varepsilon Le[R_T(1 - Le) - R^{sup}], \end{aligned}\right\} \tag{4.19}$$

and the constants R^{sup} and γ are defined by

$$R^{sup} = \frac{\mathscr{K}_\psi \; \mathscr{K}}{\mathscr{B} \; \mathscr{L}}, \quad \gamma = \frac{\mathscr{K}}{\mathscr{M}}. \tag{4.20}$$

For a square enclosure, $A = 1$, when using a grid size of 20×20, it was found that $R^{sup} = -209.84$ and $\gamma = 10.29$ for the first eigenvalue, λ_1, and $R^{sup} = -209.84$ and $\gamma = 14.70$ for the second one, λ_2.

Solving (4.18) for p, it is readily found that

$$p = p_0 \left(p_1 \pm (p_1^2 + p_2)^{1/2} \right). \tag{4.21}$$

In general, the constant p is a complex number which can be decomposed as $p = p_r + \mathrm{i}p_i$, where p_r and p_i are the real and imaginary parts respectively. From (4.21) it can be easily demonstrated that

$$\left.\begin{aligned} &\left.\begin{aligned} p_r &= p_0 \left[p_1 + (p_1^2 + p_2)^{1/2} \right] \\ p_i &= 0 \end{aligned}\right\} \quad \text{if} \quad p_1^2 + p_2 \geqslant 0, \\ &\left.\begin{aligned} p_r &= p_0 p_1 \\ p_i &= p_0 (|p_1^2 + p_2|)^{1/2} \end{aligned}\right\} \quad \text{if} \quad p_1^2 + p_2 < 0. \end{aligned}\right\} \tag{4.22}$$

According to (4.18) and (4.19) the marginal state of instability corresponds to $p = 0$, i.e. $R_{TC}(1 - Le) = R^{sup}$, in agreement with the results of (4.9).

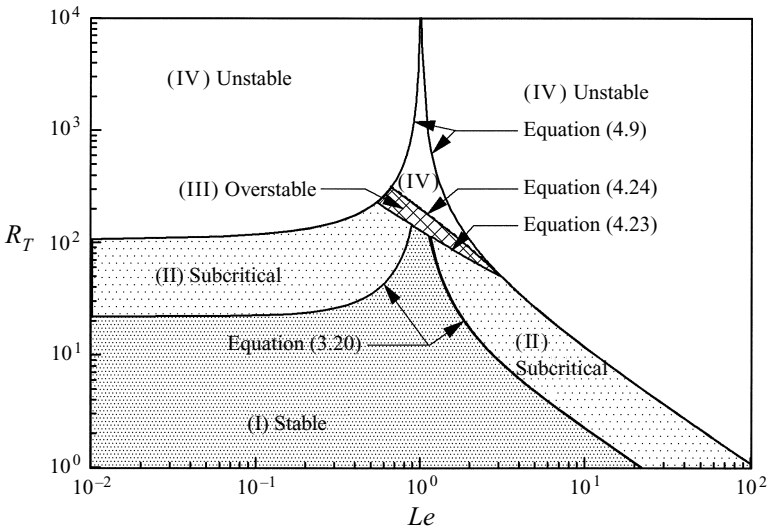

FIGURE 8. Stability diagram for an infinite vertical layer, $\varepsilon = 0.1$.

The marginal state of overstability at which the oscillatory convection may arise corresponds to $p_r = 0$ and $p_i \neq 0$, i.e. $p_1 = 0$. From (4.22) the resulting overstable critical Rayleigh number for the onset of oscillatory flows is given by

$$R_{TC}^{over} = \frac{(\varepsilon Le + 1)}{Le(\varepsilon - 1)} R^{sup}. \tag{4.23}$$

The oscillatory convective regime ($p_r \neq 0$ and $p_i \neq 0$) was found to exist up to a critical Rayleigh number R_{TC}^{osc} at which the transition from the oscillatory to direct mode occurs. In other words, an overstability exists only when the condition $p_1^2 + p_2 < 0$ is satisfied, i.e. $R_{TC}^{over} \leqslant R_T \leqslant R_{TC}^{osc}$ where the value of R_{TC}^{osc} is deduced from the condition $p_1^2 + p_2 = 0$ as

$$R_{TC}^{osc} = \frac{(\varepsilon Le - 1)}{Le(\varepsilon - 1)^2} \left[\varepsilon + 1 + 2\varepsilon^{1/2}\right] R^{sup}. \tag{4.24}$$

4.2.1. *Results and discussion*

The stability diagram for a slender vertical porous layer ($A \to \infty$), as predicted by the linear stability analysis (linear theory) and the parallel flow approximation (nonlinear theory), is presented in figure 8 for $\varepsilon = 0.1$. The diagram is presented in the (R_T, Le)-plane. Four distinct regions are delineated by the curves resulting from (3.20), (4.9), (4.23) and (4.24). In region (I) ($R_T < R_{TC}^{sub}$), below the subcritical Rayleigh number (3.20), the fluid is expected to remain stable according to both linear and nonlinear theories. Any arbitrary dynamic perturbation will evolve to a rest state. In region (II), the nonlinear theory predicts the existence of finite-amplitude convection. However, according to the linear theory, the basic rest state solution is stable. It was found that upon starting the numerical simulations with a finite-amplitude flow as initial conditions, a convective motion could be maintained above the subcritical and below the supercritical Rayleigh numbers. On the other hand, upon starting with a small-amplitude convective motion, the solution was observed to decay towards a pure conductive state. In region (III), the linear stability analysis shows that both real and imaginary parts of the parameter p, (4.21), are positive. The numerical results

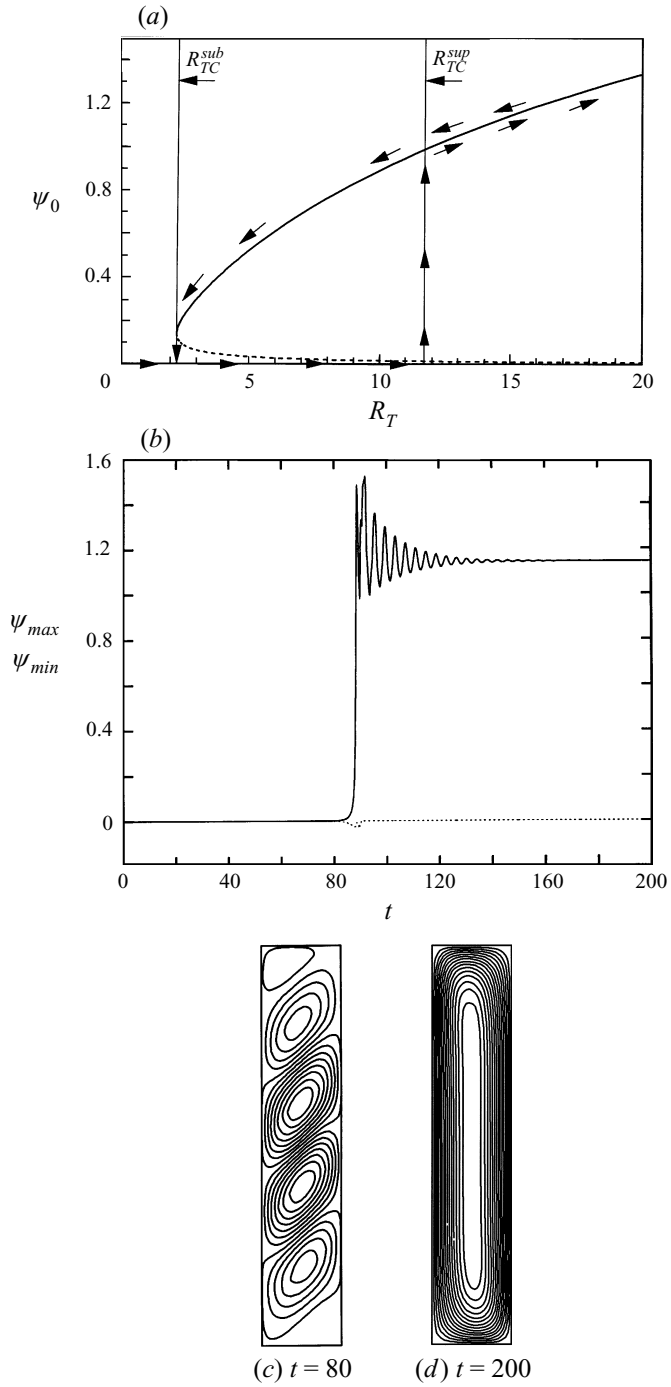

FIGURE 9. Bifurcation diagram for $Le = 10$ and $\varepsilon = 1$ (a) flow intensity, ψ_0, as a function of the thermal Rayleigh number and (b) time history of maximum and minimum stream function values for $R_T = 15$, $Le = 10$ and $A = 5$ with $\psi = 0$, $T = S = x$ as initial conditions. (c, d) streamlines.

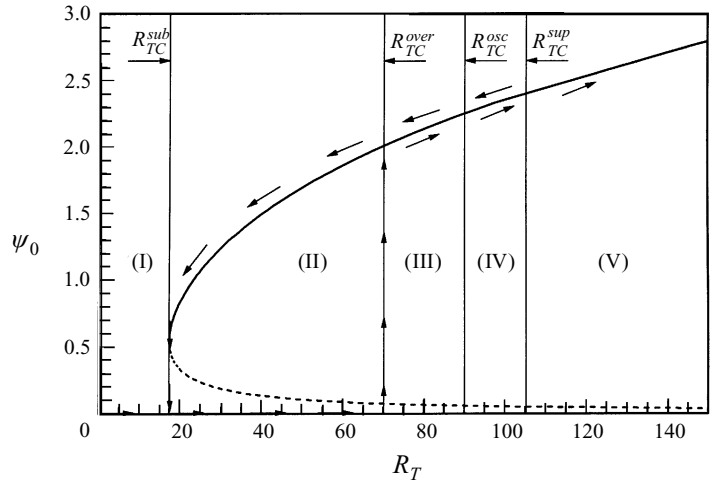

FIGURE 10. Bifurcation diagram for $Le = 2$ and $\varepsilon = 0.1$: stream function ψ_0 as a function of the thermal Rayleigh number R_T.

indicate that, upon starting the numerical simulation with the pure diffusive solution as initial conditions, the flow, temperature and concentration amplitudes grow in an oscillatory manner in this region. The extent of this region depends strongly upon the value of the normalized porosity, ε, of the porous medium. The area of region (III) is found to move up and shrink to zero as the value of ε is increased to unity. For this case, the exchange of stability is valid and the marginal state of instability is only possible via stationary convection. In region (IV), above the neutral stability line, (4.9), the system is unstable and any arbitrary dynamic perturbation can initiate a monotonic convective flow. All the numerical results obtained in region (IV) demonstrate the existence of finite-amplitude convection, independently of the initial conditions.

According to the parallel flow approximation and the linear stability analysis, for the particular case of $Le = 1$ and $\varepsilon = 1$ the supercritical Rayleigh number for the onset of motion tends towards infinity such that the system is unconditionally stable. This point is in agreement with the numerical results obtained by Trevisan & Bejan (1986). On the other hand, when the normalized porosity ε is not equal to unity, it is clear from (2.7)–(2.9) that, for $Le = 1$, the transient behaviour of the temperature and concentration fields are different from each other. As a result, the buoyancy force in the momentum equation (2.7) is non-zero such that the existence of a permanently oscillating flow is possible. This point has been confirmed numerically in the present study but the results are not presented here. For this situation, the critical Rayleigh number for the onset of convection is given by $R_{TC}^{over} = |R^{sup}|(\varepsilon + 1)/(1 - \varepsilon)$.

Figures 9 and 10 illustrate the bifurcation diagrams in term of the flow intensity as a function of the Rayleigh number, R_T, for typical values of ε and Le. The curves depicted in these graphs are the prediction of the parallel flow theory such that the results are valid for a slender cavity ($A \gg 1$). Figure 9(a) shows the results obtained when $Le = 10$ and $\varepsilon = 1$. For this case, the subcritical and supercritical Rayleigh numbers are $R_{TC}^{sub} = 2.236$ and $R_{TC}^{sup} = 11.707$ respectively. As described above, the system is stable (region I, in figure 8) when $R_T < 2.236$ and unstable (region IV) when $R_T > 11.707$. Figure 9(b–d) illustrates typical numerical results obtained for $R_T = 15$, $Le = 10$, $A = 5$ and $\varepsilon = 1$. The initial conditions for the numerical computations

were the pure diffusive state. The resulting evolution of ψ_{max} and ψ_{min}, maximum and minimum values of the stream function respectively, with time indicates that up to $t \simeq 85$ convection remains extremely weak. The flow pattern obtained at $t = 80$ indicates the formation of a periodic structure consisting of tilted counter-rotating cells similar to those predicted by the linear stability analysis (see figure 6*e*, *f*). At $t = 85$, the flow develops suddenly to yield, after the occurrence of a transitory unsteady oscillating regime, a solution that approaches the steady-state regime. For this situation, at $t = 200$, the flow exhibits parallel streamlines as predicted by the nonlinear theory. Also, it is seen from figure 9(*a*), in the range $2.236 < R_T < 11.707$ (region II), that two solutions are possible. The first one corresponds to the pure diffusive regime, $\psi = 0$, and the second one to the finite-amplitude convective regime. Which of those two modes will prevail depends essentially on the initial conditions used to start the numerical procedure.

The bifurcation diagram corresponding to $Le = 2$ and $\varepsilon = 0.1$ is presented in figure 10. For these parameters, values of the critical Rayleigh numbers are obtained as follows: $R_{TC}^{sub} = 17.360$, $R_{TC}^{over} = 70.241$, $R_{TC}^{osc} = 90.141$ and $R_{TC}^{sup} = 105.362$. Below the subcritical Rayleigh number R_{TC}^{sub}, region (I) in figure 8, the fluid is unconditionally stable and convection is impossible. In region (II), between the subcritical and overstable Rayleigh numbers, i.e. $R_{TC}^{sub} < R_T < R_{TC}^{over}$, two solutions are possible as discussed above. For the situation where $R_{TC}^{over} \leqslant R_T \leqslant R_{TC}^{osc}$ (region III in figure 8), at the beginning of convection, the flow starts to oscillate and its amplitude grows with time to bifurcate towards a finite-amplitude steady convective flow or to a periodic oscillatory one. When $R_T \geqslant R_{TC}^{osc}$ (regions IV in figure 8) the conduction state bifurcates into a monotonic convective flow (direct mode, i.e. the real part of p is positive but the imaginary part is zero). Starting with a conductive state or finite-amplitude convection as initial conditions, a hysteresis loop is indicated in figure 10 by arrows, for increasing or decreasing R_T. The analytical solution (solid line) was found to agree well with the numerical results obtained for $\varepsilon = 0.9$ and $A \geqslant 4$. As discussed before (see, for instance, figure 4), since $\varepsilon = 0.1$, the numerical converged solution was observed to oscillate with time.

The influence of the normalized porosity, ε, on the time flow history is presented in figure 11 for $A = 4$, $R_T = 50$, $Le = 5$ and different values of ε, i.e. $\varepsilon = 0.1$, 0.2 and 0.4. The rest state with uniform temperature and concentration fields ($\psi = T = S = 0$) is adopted as initial condition for the numerical computations. As may be seen from figure 11(*a*) with $\varepsilon = 0.4$, a convective flow, consisting of a single counterclockwise roll cell, bifurcates immediately from the rest state. Then, the flow intensity grows in an oscillatory manner to converge to a periodic oscillatory solution. For this case, $\varepsilon Le = 2$; as expected, right at the beginning of convection ($t > 0$) the heat diffuses more quickly than the solute since $\varepsilon\, Le > 1$. Thus the thermal gradient is established before the solutal one, giving rise to a thermally driven counterclockwise circulation ($\psi_{max} > 0$, $\psi_{min} = 0$). The thermal effects are observed to be predominant all the time. For $\varepsilon = 0.2$, figure 11(*b*) illustrates the time history of the stream function extrema. For this situation, $\varepsilon\, Le = 1$; as a result, the heat and the solute transfer rates are identical at the beginning of convection. Since $N = -1$, the buoyancy forces cancel each other and the convective flow is weakened. The numerical results for $0 < t < 1.633$ demonstrate the formation of multilayered roll cells ($\psi_{max} > 0$, $\psi_{min} < 0$) as predicted by the linear stability analysis (see figure 6*b*). By increasing t, the flow structure evolves progressively to a single counterclockwise cell. As can be observed from figure 11(*b*), the flow amplitude increases monotonically with t and then converges towards a periodic oscillatory solution. Finally, the case where $\varepsilon = 0.1$ ($\varepsilon\, Le = 0.5$) is presented

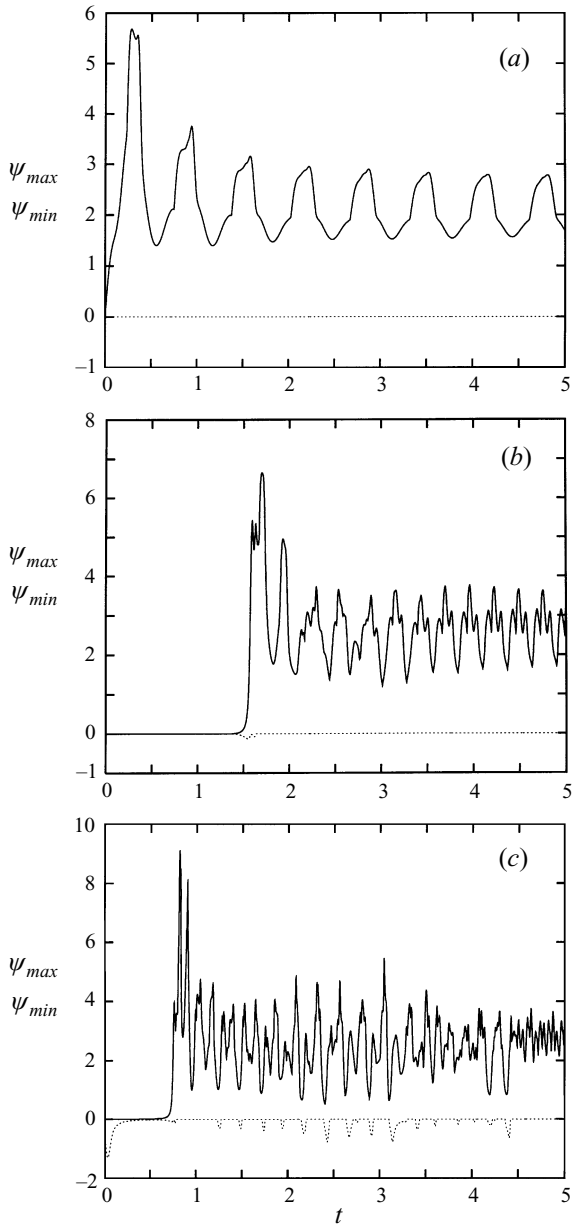

FIGURE 11. Time history of maximum and minimum stream function values for $R_T = 50$, $Le = 10$ and $A = 4$ for (*a*) $\varepsilon = 0.4$, (*b*) $\varepsilon = 0.2$, (*c*) $\varepsilon = 0.1$.

in figure 11(*c*). For this situation, $\varepsilon\, Le < 1$, hence at the beginning of convection, the faster diffusive component is the solute. As a result, a solute-driven roll cell is formed initially ($\psi_{max} = 0$, $\psi_{min} < 0$). As t increases, the flow intensity increases first, passing through a maximum at $t = 0.042$, then starts to decrease towards the rest state at $t = 0.160$. The decaying flow is due to the establishment of a thermal gradient in the enclosure which cancels progressively the solutal effects. At $t = 0.160$, multilayered roll cells are first formed. This flow structure gives rise gradually to a single thermally

driven roll cell. It seems that, according to figure 11(*c*), the solution evolves towards an oscillatory convective flow varying from single to multilayered roll cells and vice versa.

5. Conclusion

The stability of double-diffusive convection in a rectangular porous cavity, due to equal and opposing effects of horizontal gradients in temperature and solute concentration, has been studied numerically and analytically. The stability to small perturbations from the equilibrium state has been investigated using both linear and nonlinear theories. The main findings of the present investigation are

1. For the linear stability analysis, a finite element method is used to determine the critical Rayleigh numbers and the flow structures at the onset of stationary and oscillatory convection. The marginal state of instability via stationary modes is found to depend upon the Lewis number characterizing the binary fluid and the aspect ratio of the cavity. Instability via oscillatory convection (overstable mode) is also possible provided that the normalized porosity is smaller than unity. When the Lewis number is equal to unity, i.e. when the diffusivities for heat and mass are identical, an oscillatory convection is the only possible mode.

2. The stability of a tall enclosure ($A \gg 1$) has been investigated using a parallel flow approximation. The resulting nonlinear solution has demonstrated the existence of a subcritical Rayleigh number, which is a function of the Lewis number, for the onset of finite-amplitude convection. Above this critical value, the resulting steady-state solution predicted by the present theory is found to be in excellent agreement with the numerical simulations of the full governing equations. However, the numerical results reveal that this steady convection becomes unstable to an oscillatory convection as the Rayleigh number is increased above a critical value, which depends strongly upon the normalized porosity of the porous medium.

3. In practical applications, since the normalized porosity of porous media is less than unity (i.e. $0 < \varepsilon < 1$), there exists a threshold for the onset of the overstable regime even when $Le = 1$.

This work was supported in part by the Natural Sciences and Engineering Research Council, Canada and jointly by the FCAR, Government of Quebec.

REFERENCES

Alavyoon, F. 1993 On natural convection in vertical porous enclosures due to prescribed fluxes of heat and mass at the vertical boundaries. *Intl J. Heat Mass Transfer* **36**, 2479–2498.

Alavyoon, F. Masuda, Y. & Kimura, S. 1994 On natural convection in vertical porous enclosures due to opposing fluxes of heat and mass prescribed at the vertical walls. *Intl J. Heat Mass Transfer* **37**, 195–206.

Bergman, T. L. & Shrinivasan, R. 1989 Numerical simulation of Soret-induced double diffusion in an initially uniform concentration binary fluid. *Intl J. Heat Mass Transfer* **32**, 679–687.

De Groot, S. R. & Mazur, P. 1962 *Non Equilibrium Thermodynamics*. North Holland.

Gobin, D. & Bennacer, R. 1994 Double-diffusion convection in a vertical fluid layer: onset of the convection regime. *Phys. Fluids* **6**, 59–67.

Goyeau, B., Songbe, J. P. & Gobin, D. 1996 Numerical study of double-diffusive convection in a porous cavity using Darcy-Brinkman formulation. *J. Heat Mass Transfer* **39**, 1363–1378.

Huebner, K. H, Thornton, E. A. & Byrom, T. G. 1995 *The Finite Element Method for Engineers*. John Wiley.

Kimura, S., Vynnycky, M. & Alavyoon, F. 1995 Unicellular natural circulation in a shallow horizontal porous layer heated from below by a constant flux. *J. Fluid Mech.* **294**, 231–257.

KRISHNAN, R. 1989 A numerical study of the instability of double-diffusive convection in a square enclosure with horizontal temperature and concentration gradients. *Heat Transfer in Convective Flows (HTD ASME National Heat Transfer Conference, Philadelphia)*, Vol. 107, pp. 357–368.

LIN, D. 1993 Unsteady natural convection heat and mass transfer in a saturated porous enclosure. *Wärme-und Stoffübertragung* **28**, 49–56.

MAMOU, M. 1998 Convection thermosolutale dans des milieux poreux et fluides confinés. PhD Thesis, Ecole Polytechnique of Montreal, University of Montreal, Quebec, Canada.

MAMOU, M., VASSEUR, P. & BILGEN, E. 1996 Analytical and Numerical Study of Double Diffusive Convection in a Vertical Enclosure. *Wärme-und Stoffübertragung* **32**, 115–125.

MAMOU, M., VASSEUR, P. & BILGEN, E. 1995*a* Multiple solutions for double-diffusive convection in a vertical porous enclosure. *Intl J. Heat Mass Transfer* **38**, 1787–1798.

MAMOU, M., VASSEUR, P., BILGEN, E. & GOBIN, D. 1995*b* Double-diffusive convection in an inclined slot filled with porous medium. *Eur. J. Mech.* B/*Fluids* **14**, 629–652.

MEHTA, K. N. & NANDAKUMAR, K. 1987 Natural convection with combined heat and mass transfer buoyancy effects in non-homogeneous porous medium. *Intl J. Heat Mass Transfer* **30**, 2651–2656.

NGUYEN, H. D., PACK, S. & DOUGLASS, R. W. 1994 Study of double-diffusive convection in a layered anisotropic porous medium. *Numer. Heat Transfer* B **26**, 489–505.

NIELD, D. A. 1968 Onset of thermohaline convection in porous medium. *Water Resour. Res.* **4**, 553–560.

NIELD, D. A. & BEJAN, A. 1992 *Convection in Porous Media.* Springer.

NITHIARASU, P., SEETHARAMU, K. N. & SUNDARARAJAN, T. 1996 Double-diffusive natural convection in an enclosure filled with fluid-saturated porous medium: a generalized non-Darcy approach. *Numer. Heat Transfer* A **30**, 430–426.

TREVISAN, O. V. & BEJAN, A. 1985 Natural convection with combined heat and mass transfer buoyancy effects in porous medium. *Intl J. Heat Mass Transfer* **29**, 403–415.

TREVISAN, O. V. & BEJAN, A. 1986 Mass and heat transfer by natural convection in a vertical slot filled with porous medium. *Intl J. Heat Mass Transfer* **29**, 403–415.

VASSEUR, P., ROBILLARD, L. & SEN, M. 1989 The Brinkman model for natural convection in a shallow porous cavity with uniform heat flux. *Numer. Heat Transfer* **15**, 221–242.